CHEMISTRY OF MATERIALS

pubs.acs.org/cm

Article

Outstanding Oxygen Reduction Reaction Catalytic Performance of In−PtNi Octahedral Nanoparticles Designed via Computational Dopant Screening

Jeonghoon Lim,[§] Kihyun Shin,[§] Junu Bak,[§] JeongHan Roh, SangJae Lee, Graeme Henkelman,* and EunAe Cho*

Cite This: *Chem. Mater.* 2021, 33, 8895−8903

Read Online

ACCESS | Metrics & More | Article Recommendations | Supporting Information

ABSTRACT: PtNi octahedral nanoparticles are considered as one of the best-performing catalysts for the oxygen reduction reaction (ORR). However, Ni dissolution deteriorates their catalytic activity and stability during the ORR. Here, we report a strategy that improves the ORR activity and stability of the PtNi octahedral nanoparticle catalyst through the incorporation of a novel dopant. Computational screening with seven different elements (Bi, In, Ru, Sn, Te, Zn, and Zr) suggests In as the most promising candidate based on the metal doping energy and the OH* adsorption energy. Consideration of the OH* coverage and Ni diffusion energy demonstrates the superior ORR activity and stability of the In-doped PtNi(111) structure. The calculation results were validated by synthesizing In-doped PtNi octahedral nanoparticles on a carbon support (In−PtNi/C). In−PtNi/C demonstrated excellent ORR performance outcomes (1.36 A mg_{Pt}^{-1} and 2.64 mA cm^{-2}@0.9 V_{RHE}), which were 2.1 and 7.9 times higher in terms of the mass activity and 2.4 and 13.4 times higher in terms of the specific activity compared to PtNi/C and Pt/C, respectively. After 12k potential cycles, In−PtNi/C showed excellent stability with high Ni retention; 2.4 and 43% of Ni were lost from In−PtNi/C and PtNi/C, respectively. Computational and experimental investigation demonstrates that surface-doped In creates a new active site toward the ORR and blocks Ni diffusion to the surface by making Pt less oxophilic.

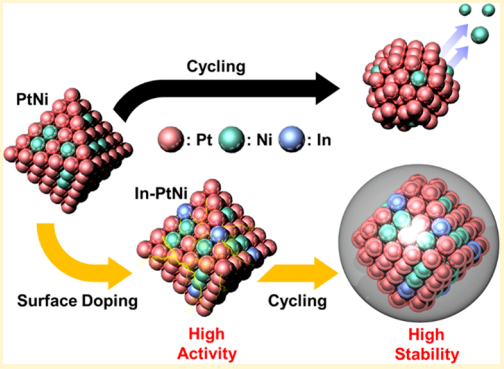

INTRODUCTION

Platinum (Pt) is the industry-standard electrocatalyst for the oxygen reduction reaction (ORR) in polymer electrolyte membrane fuel cells (PEMFCs). Pt enhances the ORR kinetics the most among mono-metallic catalysts by lowering the activation energy in the cathodic reaction.[1,2] However, Pt is an expensive noble metal with limited availability. Thus, in order to reduce Pt loadings, strategies for Pt nanostructural engineering have been extensively studied, such as alloying with transition metals (e.g., M: Ni,[3,4] Co,[5−7] Fe,[8] and others[9]) and controlling the shape of the PtM alloy nanoparticles.[4,10,11] Although many PtM alloys have demonstrated faster ORR kinetics than pure Pt owing to the modulated adsorption energy of oxygen intermediates, stability of the transition metals is one of the crucial concerns that hinders their commercial applications.[12,13]

Modifying the surfaces of PtM alloys represents a promising means by which to suppress the dissolution of the transition metals and thereby enhance their stability.[12] In particular, the surface doping of Fe,[14] Mo,[15,16] Ga,[17] and Rh[18] into PtNi octahedral nanoparticles can effectively improve their stability and ORR activity as well. Nonetheless, PtM alloy catalysts have scarcely been applied to PEMFC systems. To boost the practical use of PtM alloy catalysts, it is necessary to establish a dopant-selection process for efficient catalyst development. A good way to explore dopant candidates is to utilize density functional theory (DFT) calculations, which are now widely used to design feasible electrochemical catalysts.[19−28]

In this study, we present a promising dopant, indium (In), via a computational screening process based on the metal doping energy and the OH* adsorption energy. By taking the factors of the OH* coverage and Ni diffusion energy into consideration, the superior ORR activity and durability of In−PtNi(111) surface are theoretically demonstrated. Surface-doped In atoms modulate the OH* adsorption energy of the first nearest neighbor Pt atoms, thereby creating highly active sites for the ORR. In accordance with the DFT calculation results, In-doped PtNi octahedral nanoparticles synthesized on

Received: September 15, 2021
Revised: October 20, 2021
Published: November 1, 2021

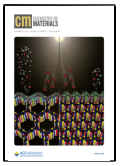

https://doi.org/10.1021/acs.chemmater.1c03196
Chem. Mater. 2021, 33, 8895−8903

a carbon support (In−PtNi/C) exhibit excellent ORR activity and shape stability with high Ni retention. Transmission electron microscopy (TEM), energy-dispersive spectrometry (EDS), and X-ray absorption near-edge structure (XANES) analyses were conducted to investigate the effects of the In dopant on the properties of PtNi octahedral nanoparticles.

METHODS

Computational Methods. GGA-level, spin-polarized DFT calculations were performed with the Vienna ab initio simulation package using a plane wave basis set with a cut-off energy of 400 eV. The revised Perdew−Burke−Ernzerhof functional was used to describe the electron exchange and correlation.[29−31] The Brillouin zone was sampled with a 2 × 2 × 1 *k*-point mesh following the Monkhorst−Pack scheme. The convergence criteria for electronic and geometric optimization were 10^{-5} eV and 0.01 eV/Å, respectively.

Metal-doped PtNi (Pt/Ni = 2:1) surface slabs were modeled with the doping elements of Bi, In, Ru, Sn, Te, and Zn, as shown in Figure S1. The slabs had a 20 Å vacuum gap in the *z*-direction; the bottom two atomic layers were fixed in their bulk positions. To predict the ORR activity, we considered the OH* adsorption energy as the descriptor has been widely used in many ORR studies, including our previous work.[23,25,32−35] We also calculated the metal doping energy to select the most stable doping metal among the six elements considered. The adsorption energy and doping energy were calculated as

$$\Delta E_{ads.} = \Delta E_{slab+mol.} - \Delta E_{slab} - \Delta E_{mol.} \quad (1)$$

$$\Delta E_{dop.} = (\Delta E_{M\text{-}PtNi} + \Delta E_{bulk\_Pt\ or\ Ni}) - (\Delta E_{PtNi} + \Delta E_{bulk\_In}) \quad (2)$$

where $\Delta E_{ads.}$ is the adsorption energy, $\Delta E_{slab+mol.}$ is the energy after adsorption, ΔE_{slab} is the energy of the clean surface, and $\Delta E_{mol.}$ is the energy of the gas molecule. For the calculation of OH* adsorption energy, there are two options for the reference value ($\Delta E_{mol.}$); $H_2O(g) - 0.5H_2(g)$ and $0.5O_2(g) + 0.5H_2(g)$. Here, we used gas energy of $[H_2O(g) - 0.5H_2(g)]$ as a reference for the calculation of OH* adsorption energy. Then, OH* adsorption energy is calculated as positive, and a greater value of positive OH* adsorption energy corresponds to weaker adsorption. $\Delta E_{dop.}$ is the doping energy, $\Delta E_{M\text{-}PtNi}$ is the total energy of the M-doped PtNi slab, and ΔE_{PtNi} is the total energy of the undoped PtNi slab. ΔE_{bulk_Pt}, ΔE_{bulk_Ni}, and ΔE_{bulk_In} are energies of single Pt, Ni, or In atom in their stable elemental bulk structure, respectively. For the In−PtNi system in which In atom replaced Pt or Ni atom, ΔE_{bulk_Pt} or ΔE_{bulk_Ni} was used to calculate the doping energy, respectively.

Experimental Methods. *Chemicals and Materials.* Platinum(II) acetylacetonate [$Pt(acac)_2$, 97%], nickel(II) acetylacetonate [$Ni(acac)_2$, 95%], indium(III) acetylacetonate [$In(acac)_3$, ≥99.99%], benzoic acid (C_6H_5COOH, 99%), *N*,*N*-dimethylformamide (DMF) were purchased from Sigma-Aldrich. Vulcan Carbon (XC-72R) was purchased from Cabot Corporation. Commercial Pt/C (Tanaka Co. 46 wt %, 2−5 nm Pt nanoparticles) was used as a reference catalyst in this study.

Synthesis of PtNi/C. The PtNi octahedral nanoparticles on the carbon support (PtNi/C) were synthesized by a one-pot method whereby all chemical materials were developed in one reactor, as described below. $Pt(acac)_2$ (8 mg) and $Ni(acac)_2$ (4 mg) were used as precursors with an atomic ratio of Pt to Ni of 1.5. Benzoic acid (C_6H_5COOH, 122 mg) was used as a shape-directing agent, and Vulcan Carbon XC-72R (20 mg) was used as the catalyst support. All chemicals were dissolved in DMF (10 mL), and the carbon support was added to the solution. The mixture was dispersed by ultrasonication for at least 30 min. The suspension was placed in an oil bath that was heated to 160 °C, stirred vigorously for 12 h, and then cooled to room temperature. The resulting products were collected by centrifugation (8000 rpm) five times using ethanol and cyclohexane and then dried in a vacuum oven at 60 °C for 12 h.

Synthesis of In-Doped PtNi/C (In−PtNi/C). The prepared PtNi/C (20 mg) samples were dispersed in 10 mL of DMF, and $In(acac)_3$ was added to the PtNi/C suspension. The amount of $In(acac)_3$ was determined to be 3 at. % In with respect to the Pt and Ni total in PtNi/C. The mixture was ultrasonicated for 30 min and then placed in an oil bath at 170 °C for 48 h with vigorous stirring before cooling to room temperature. The resulting mixture was collected by centrifugation five times using an ethanol and cyclohexane mixture and then dried in a vacuum oven at 60 °C for 12 h.

Characterization. TEM (JEOL 2000 FX), Cs-corrected high-resolution TEM (HRTEM, Titan cubed G2 60-300, 300 kV), and high-angle annular dark-field scanning TEM (STEM) images were obtained to confirm the morphology and crystal structure of the In−PtNi/C and PtNi/C. Energy-dispersive X-ray spectroscopy was conducted with Cs-corrected TEM measurements to explore the chemical composition and elemental distributions. Inductively coupled plasma optical emission spectroscopy (ICP−OES, Agilent 7700S) was also used to determine the overall chemical compositions. X-ray powder diffraction (XRD) patterns using Cu Kα radiation and XANES spectroscopy were utilized to examine the crystal structure and electronic structure, including the oxidation states of Pt. The XANES measurements were performed at the 8C nano-probe XAFS beamline (BL8C) of the Pohang Light Source (PLS-II) in a 3.0 GeV storage ring (current of 360 mA). This radiation source is a tapered in-vacuum undulator, and the XANES spectra were collected in both transmission and fluorescence modes.

Electrochemical Measurements. Half-cell tests were conducted using a potentiostat (Pine Instruments) with a conventional rotating disk electrode measurement in a three-electrode electrochemical cell. The catalyst inks were prepared by dispersing catalyst powders and a 5 wt % Nafion solution (1100 W, DuPont, 20 μL) in a deionized water (0.5 mL)/isopropyl alcohol (0.5 mL) solution. After ultrasonication for 30 min, the well-dispersed catalyst ink was coated onto the surface of a glassy carbon electrode (GCE) as the working electrode. The Pt loading of all catalysts on the GCEs was 25 μg_{Pt} cm^{-2}, and each sample was dried at room temperature in air. A Pt mesh and saturated calomel electrode were used as the counter and reference electrode, respectively. All potentials were reported with respect to a reversible hydrogen electrode (RHE).

All electrochemical measurement data were collected after stabilizing the catalysts coated onto the GCE. As an electrochemical pre-treatment, 100 potential cycles were conducted in the potential range from 0.05 to 1.1 V_{RHE} at a scan rate of 50 mV s^{-1} without rotating the electrode. The electrochemical active surface area (ECSA) was estimated using the hydrogen under potential deposition (HUPD) and the CO stripping method. For HUPD, the cyclic voltammograms (CVs) were obtained in an Ar-saturated 0.1 M $HClO_4$ electrolyte with a scan rate of 50 mV s^{-1} at room temperature. The $ECSA_{HUPD}$ was estimated by integrating the hydrogen adsorption/desorption charge area between 0.05 and 0.35 V_{RHE}. For CO stripping, the catalyst-coated GCE was immersed in a 0.1 M $HClO_4$ solution, and the solution was purged with in the sequence of Ar, CO, and Ar for 10 min, respectively. Then, two cycles of cyclic voltammetry were performed with a scan rate of 20 mV s^{-1} from 0.05 to 1.1 V_{RHE}. The CO desorption peak was integrated to calculate $ECSA_{CO}$. The ORR performance was measured by linear sweep voltammetry (LSV) in an O_2-saturated 0.1 M $HClO_4$ electrolyte using a scan rate of 10 mV s^{-1} from 0.05 to 1.1 V_{RHE} at 1600 rpm. After repeating the potential sweeping 10 times, the stabilized ORR LSV data were collected and presented. The catalyst durability was estimated by means of an accelerated stress test in an O_2-purged 0.1 M $HClO_4$ electrolyte via repeated potential cycling between 0.6 and 1.1 V_{RHE} at a scan rate of 50 mV s^{-1}. CVs and ORR polarization curves were acquired after 4k, 8k, and 12k potential cycles. Koutecky−Levich equation was used to calculate the kinetic current considering the mass transport limitation. The electron transfer number (n) of In−PtNi/C was obtained from the ORR polarization curves measured with different rotating speeds from 400 to 1600 rpm, using the Koutechy−Levich equation

https://doi.org/10.1021/acs.chemmater.1c03196
Chem. Mater. 2021, 33, 8895−8903

$$\frac{1}{j} = \frac{1}{j_K} + \frac{1}{j_L} = \frac{1}{B}\omega^{-1/2} + \frac{1}{j_K}$$

where j, j_K, and j_L are the measured, kinetic, and diffusion-limiting current densities, respectively. j_L is proportional to the square root of angular velocity (ω) of the RDE. The proportionality coefficient (B) is

$$B = 0.62D^{2/3}\nu^{-1/6}nFC_{O_2}$$

where D is the diffusion coefficient of O_2 in 0.1 M $HClO_4$ solution (1.93×10^{-5} cm^2 s^{-1}), ν is the kinematic viscosity of the electrolyte (1.01×10^{-2} cm^2 s^{-1}), n is the number of electrons transferred, F is Faraday's constant (96,485 C mol^{-1}), and C_{O_2} is the concentration of molecular oxygen in 0.1 M $HClO_4$ solution (1.26×10^{-6} mol cm^{-3}).[36]

The rotating ring-disk electrode (RRDE) method was conducted to verify the electron transfer number and H_2O_2 yield. The electron transfer number (n) and H_2O_2 yield (p) can be calculated from the disk current (i_d) and ring current (i_r) using below equations[36]

$$n = 4 \times \frac{i_d}{i_d + \frac{i_r}{N_c}}, \quad p = 2 \times \frac{\frac{i_r}{N_C}}{i_d + \frac{i_r}{N_c}}$$

where N_C is the collection efficiency of the RRDE (37%).

RESULTS AND DISCUSSION

Screening of Doping Elements. To design novel catalysts for the ORR, a PtNi(111) system (Pt/Ni = 2:1) was constructed with a Pt skin layer (Figure S1a,b). It is generally considered that non-noble metals on the surfaces of Pt-based alloys dissolve in an acidic PEMFC environment, forming a Pt-enriched surface layer.[37−40] To find a novel dopant for the PtNi(111) system, seven different elements (M: Bi, In, Ru, Sn, Te, Zn, and Zr), not investigated in previous studies,[41−46] were selected as candidates. Each element was doped into four different sites of the PtNi structure; two in the surface layer with corresponding Ni-rich and Pt-rich sub-surface layer configurations (Figure S1c,d), denoted as ("Ni-rich" and "Pt-rich", respectively), and two in the sub-surface layer replacing the Pt and Ni sites.

For the M-doped PtNi(111) systems, the structural stability and ORR activity were investigated as the first screening considerations. The structural stability was determined from the metal doping energy, defined as the energy difference between the PtNi and M-doped PtNi slabs. The OH* adsorption energy was used as an ORR activity descriptor as either the first step [$O_2(g) \rightarrow$ OOH*] or the last step [OH* $\rightarrow H_2O(l)$] is typically the rate-determining step of the ORR.[32,33] In addition, the OH* and OOH* adsorption energies have a linear correlation,[47−49] meaning that the ORR activity can be described using the OH* adsorption energy.

The calculated metal doping energy and OH* adsorption energy are plotted in Figure 1 with the well-known "top of the volcano curve" that indicates the optimal OH* adsorption energy for the ORR.[47] The primary purpose of this process was to screen the doping elements for the PtNi(111) system using simple descriptors. Although both the activity and stability of a catalyst are of equal importance, we first focused on the stability since M-doping aims to improve stability of the PtNi system.[18,50,51] Figure 1 shows that In, Sn, Zn, or Zr-doped PtNi can be stably synthesized with the negative doping energies for all the four types of doping sites. On the other hand, Ru, Te, or Bi-doped PtNi exhibit positive doping energies for at least two types of the doping sites. These results

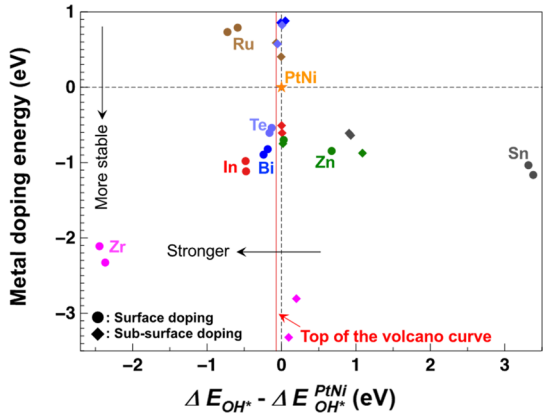

Figure 1. Screening of doping elements based on the metal doping energy and OH* adsorption energy, as compared to the reference of PtNi. The vertical line shown in red represents the OH* adsorption energy corresponding to the top of the ORR volcano derived from linear scaling relationships.[33,47]

imply that Ru, Te, or Bi-doped PtNi might be synthesized but their effectiveness as promoters are likely reduced due to the structural instability. Thus, Ru, Te, and Bi were excluded from the dopant candidates. Among the first-screened doping elements (In, Sn, Zn, and Zr), In exhibits the OH* adsorption energies closest to the optimal OH* adsorption energy (volcano top). As a result, In was selected as the primary dopant candidate, and the In-doped PtNi(111) system was investigated theoretically and experimentally.

Activity and Durability Calculations of In−PtNi(111). For the In−PtNi(111) system, surface doping sites are found to be more stable than sub-surface doping sites (Figure 1), implying that In atoms would be primarily positioned in the surface layer of synthesized PtNi octahedral nanoparticles. Thus, the ORR activity of the surface-doped In−PtNi(111) (Figure S1c,d) was further examined in comparison to the ORR activity of PtNi(111) and Pt(111).

For the calculation of OH* adsorption energy, gas energy of [$H_2O(g) - 0.5H_2(g)$] was used as a reference, which has been widely employed in DFT studies.[23−25,52] With respect to the reference energy, OH* adsorption energies of precious metals are represented as positive,[47,52] and a greater value of positive OH* adsorption energy means weaker adsorption. For the surface-doped In−PtNi(111) structures with either Ni-rich (Figure S1c) or Pt-rich (Figure S1d) doping sites, the strongest OH* adsorption site was found to be on top of the In atom (Figure S2). As the OH* adsorption site moves far from the In atom, the OH* adsorption becomes weaker monotonically on the first and the second nearest neighbor (1NN and 2NN) Pt atoms. These outcomes imply that OH* would be preferentially adsorbed on top of the surface-doped In atoms of In−PtNi(111).

Then, the surface OH* coverage was considered since the cathode catalyst surface is partially covered with adsorbed OH* during fuel cell operation,[53−55] and the OH* adsorption energy is affected by pre-adsorbed OH*. In addition, adsorbed OH* can stay on the In atom owing to the strong adsorption energy. Figure 2 presents the adsorption energies for the first (1OH*), second (2OH*), and third OH* adsorption (3OH*) on In−PtNi(111), PtNi(111), and Pt(111). Following 1OH* adsorption on top of In atom (Figure S2), adsorption sites for 2OH* and 3OH* are representatively illustrated in inset of

https://doi.org/10.1021/acs.chemmater.1c03196
Chem. Mater. 2021, 33, 8895−8903

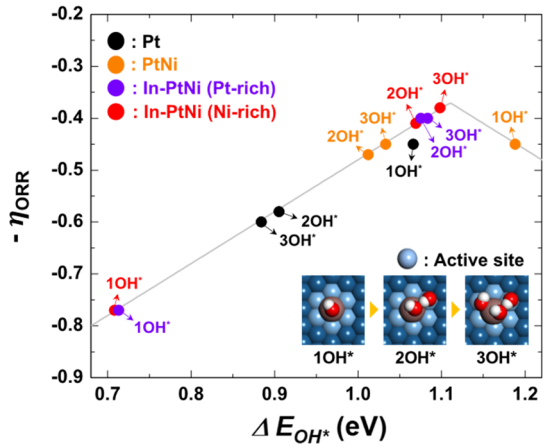

Figure 2. ORR volcano plot as a function of the OH adsorption energy on Pt (black), PtNi (orange), In−PtNi (Pt-rich, purple), and In−PtNi (Ni-rich, red). Inset figure shows the OH* adsorption configuration and the most ORR-active sites (light blue) created by the doped In atom (brown) of In−PtNi(111).

Figure 2. The OH* adsorption on Pt (1OH*: 1.066, 2OH*: 0.905, and 3OH*: 0.884 eV) and PtNi (1OH*: 1.188, 2OH*: 1.012, and 3OH*: 1.033 eV) mostly becomes stronger with OH* coverage, due to the hydrogen bonding between the adsorbed OH* species. Interestingly, the OH* adsorption energy on In−PtNi shows a unique response to the OH* coverage; the OH* adsorption on In−PtNi becomes weaker with OH* coverage (1OH*: 0.708, 2OH*: 1.068, and 3OH*: 1.098 eV for Ni-rich site and 1OH*: 0.713, 2OH*: 1.075, and 3OH*: 1.083 eV for Pt-rich site). Furthermore, it is noteworthy that In−PtNi(111) has the 3OH* adsorption energies very close to the optimal value with the highest levels of ORR activity on the volcano plot. The sub-surface layer configuration has a minimal effect on the 3OH* adsorption energy and ORR activity.

In general, 1OH* adsorption energy is used as an ORR activity descriptor. For Pt(111) and PtNi(111), the 1OH* adsorption energy is closer to the optimal value compared to the 2OH* and 3OH* adsorption energies. Thus, 1OH* produces the highest ORR activity, and 1OH* adsorption energy can be a suitable descriptor. However, for the In−PtNi(111) system, 3OH* adsorption energies are closer to the optimal value than the strongly adsorbed 1OH* and 2OH*, leading to the highest ORR activity. These results reveal that OH* coverage should be taken into consideration to describe the ORR activity of In−PtNi. In addition, we calculated surface diagrams[54] for Pt, Pt_2Ni, In−Pt_2Ni (Pt-rich), and In−Pt_2Ni (Ni-rich) with 1OH*, 2OH*, and 3OH* (Figure S3). As widely observed and also shown in Figure 5 below, the ORR starts at potential approximately 0.95−1.00 V_{RHE}. The surface diagrams demonstrate that 3OH* is the most stable at potentials above 0.85 V_{RHE} for all the systems. These outcomes imply that Pt, Pt_2Ni, In−Pt_2Ni (Pt-rich), and In−Pt_2Ni (Ni-rich) are most stable with 3OH* in the potential region where ORR starts. It should be pointed out that 3OH* on In−PtNi(111) exhibits the closest adsorption energy to the optimal value among all the calculated OH* adsorption energies for In−PtNi, PtNi, and Pt. Furthermore, doped In makes the first nearest neighbor (1NN) Pt have OH* adsorption energy very close to the optimal value, creating highly active sites for the ORR (inset of Figure 2).

Durability is another crucial issue associated with ORR catalysts. Degradation of PtNi(111) catalysts has been closely linked to the dissolution of Ni.[18,51] As schematically illustrated in Figure S4a, Ni diffusion from the sub-surface to the surface layer results in Ni dissolution because Ni on the surface layer would be readily leached into the acidic electrolyte. Thus, the diffusion energy was defined as the energy difference before and after the diffusion of the Ni or Pt atom from the sub-surface to the surface layer. As shown in Figure 3, Ni diffusion

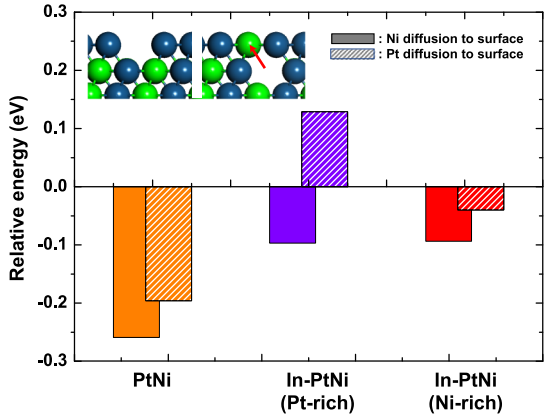

Figure 3. Diffusion energy of Ni and Pt atoms from the sub-surface to the surface in the PtNi and In−PtNi systems.

is more favorable than Pt diffusion for In−PtNi (Pt-rich), In−PtNi (Ni-rich), and PtNi. However, the Ni diffusion energies in In−PtNi (−0.097 and −0.094 eV for the Pt-rich and Ni-rich configuration, respectively) are significantly reduced compared to that in PtNi (−0.259 eV). Thus, the presence of In can suppress Ni diffusion to the surface and hence improve the durability of the PtNi(111) catalyst. All of these DFT calculation results propose that In doping can significantly enhance the ORR activity and durability of PtNi(111). Next, we synthesize In−PtNi octahedral nanoparticles to confirm these computational results.

Material Characterization. The HRTEM and STEM images in Figure 4 reveal well-distributed In−PtNi and PtNi octahedral single-crystal nanoparticles with an average edge length of 6.0 ± 0.4 nm and an edge lattice spacing of 0.22 nm.

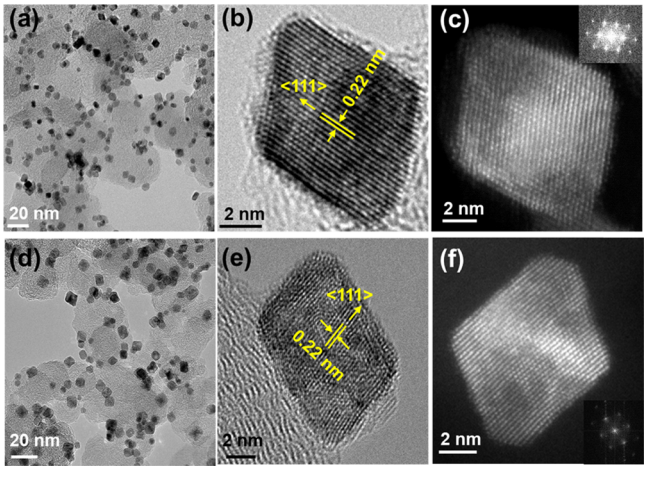

Figure 4. HRTEM and STEM images of (a−c) In−PtNi/C and (d−f) PtNi/C.

https://doi.org/10.1021/acs.chemmater.1c03196
Chem. Mater. 2021, 33, 8895−8903

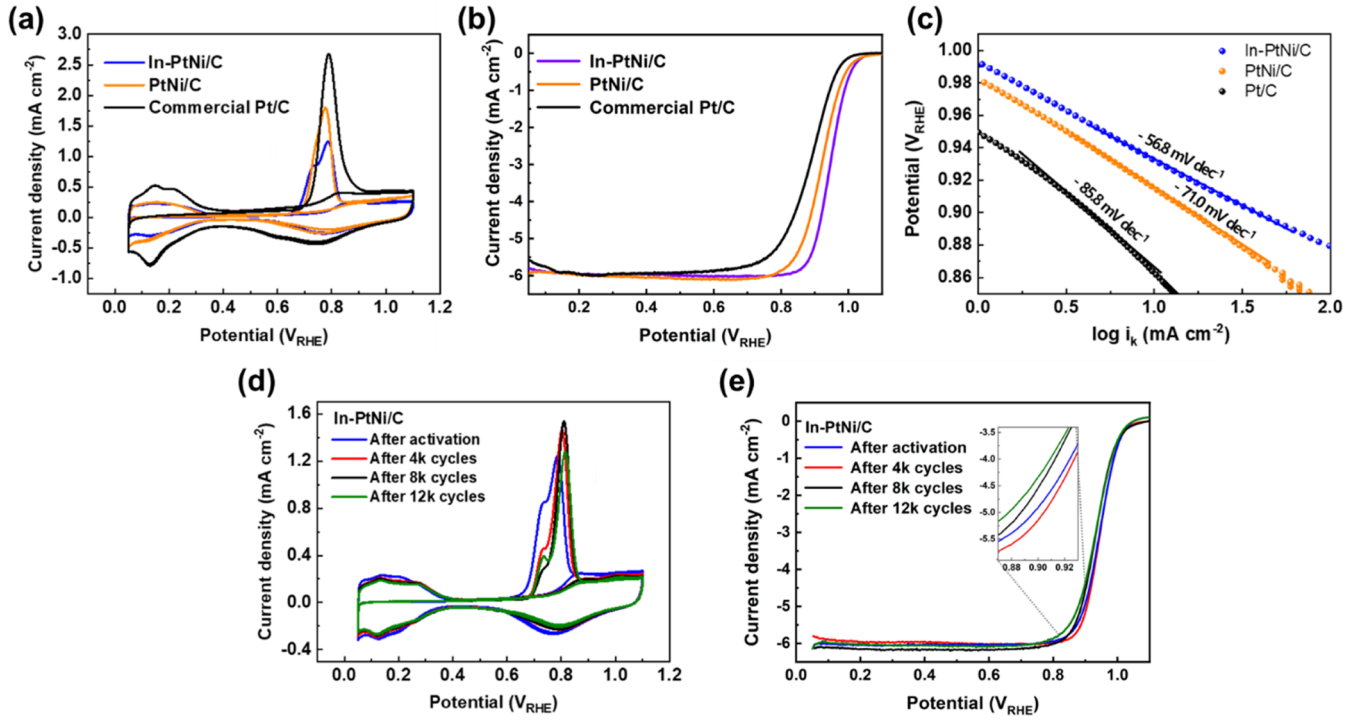

Figure 5. (a) CO stripping voltammograms and (b) ORR polarization curves of In−PtNi/C, PtNi/C, and commercial Pt/C. (c) Tafel plots for In−PtNi/C, PtNi/C, and Pt/C. (d) CO stripping voltammograms and (e) ORR polarization curves measured before and after 4k, 8k, and 12k potential cycles from 0.6 to 1.1 V_{RHE}; the inset is an enlargement of the potential range near 0.9 V_{RHE}.

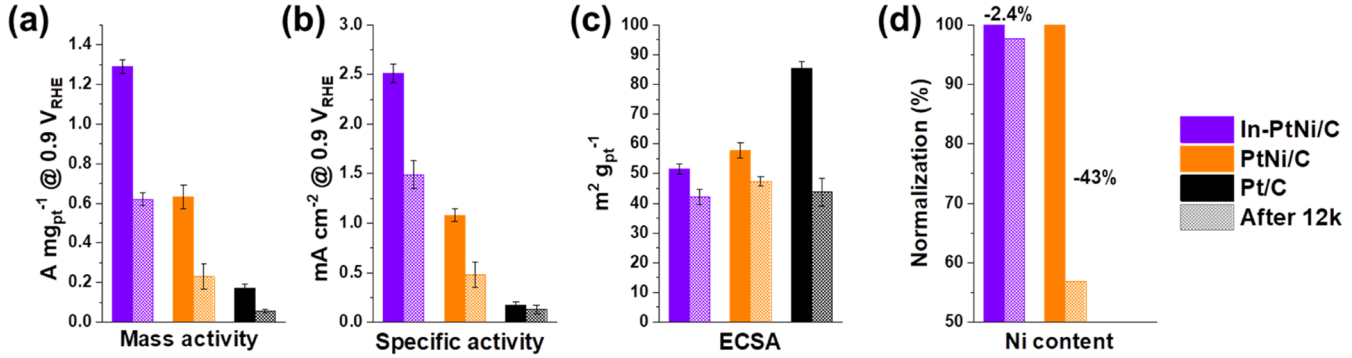

Figure 6. (a) Mass activity, (b) specific activity, and (c) ECSA of In−PtNi/C, PtNi/C, and commercial Pt/C before and after 12k cycles. (d) Normalized Ni content (at. %) in In−PtNi/C and PtNi/C before after 12k cycles calculated from the results, as shown in Figures S8−S11.

Incorporating In metal has negligible effects on the crystal structure of PtNi octahedral nanoparticles (Figures 4 and S5), whose (111) facet is widely known to have the highest ORR activity.[50] Table S1 summarizes the chemical compositions of In−PtNi/C and PtNi/C, as measured by ICP−OES. The atomic ratio of Pt to Ni was approximately 1.4−1.5 in both samples with 1.6 at. % In in In−PtNi/C.

Electrochemical Performance of In−PtNi Nanoparticles. The ECSAs of In−PtNi/C, PtNi/C, and commercial Pt/C were measured using HUPD and CO stripping methods (Figures 5a and S6a). In−PtNi/C and PtNi/C exhibit similar ECSAs with HUPD (30.8 and 30.2 $m^2\ g_{Pt}^{-1}$, respectively) and CO stripping (51.4 and 57.7 $m^2\ g_{Pt}^{-1}$, respectively). The ECSA of the commercial Pt/C was found to be 79.4 $m^2\ g_{Pt}^{-1}$ obtained from HUPD and 87.1 $m^2\ g_{Pt}^{-1}$ obtained from CO stripping, respectively (Table S2). $ECSA_{HUPD}$ values of In−PtNi/C and PtNi/C were lower than corresponding $ECSA_{CO}$ values, due to the suppression effect of alloyed Ni on the HUPD.[56,57] The ECSAs of In−PtNi/C and PtNi/C, smaller than commercial Pt/C, are related to the larger nanoparticle sizes (Figures 4 and S7a,c). Figure 5b shows that the initial ORR performance of the catalysts increases in the following order: Pt/C < PtNi/C < In−PtNi/C. From the data, as shown in Figure 5a,b, the mass activities were calculated with specific activities based on $ECSA_{CO}$ (Table S3). In terms of the mass activity, In−PtNi/C showed an outstanding ORR performance (1.36 A mg_{Pt}^{-1}@0.9 V_{RHE}), showing a 2.1-fold enhancement from PtNi/C (0.640 A mg_{Pt}^{-1}@0.9 V_{RHE}) and a 7.9-fold enhancement in comparison with commercial Pt/C (0.172 A mg_{Pt}^{-1}@0.9 V_{RHE}). The specific activity of In−PtNi/C (2.64 mA cm^{-2}@0.9 V_{RHE}) is 2.4 times higher than that of PtNi/C (1.11 mA cm^{-2}@0.9 V_{RHE}) and 13.4 times higher than that of commercial Pt/C (0.197 mA cm^{-2}@0.9 V_{RHE}). These ORR performance of In−PtNi/C is compared to the previously reported metal-doped PtNi/C (Table S4). In addition, In−PtNi/C showed a lower Tafel slope (−56.8 mV dec^{-1}) than

https://doi.org/10.1021/acs.chemmater.1c03196
Chem. Mater. 2021, 33, 8895−8903

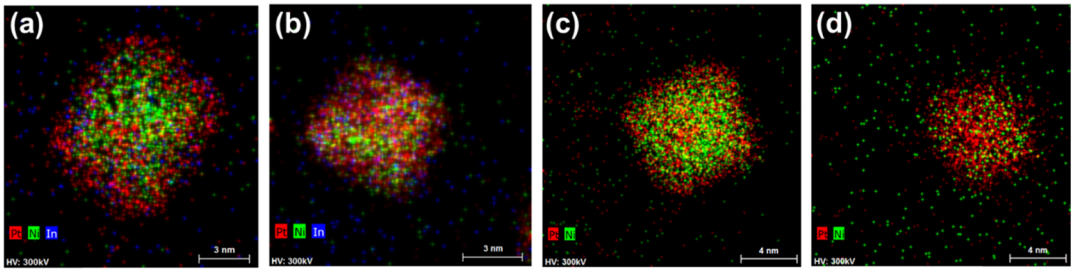

	wt %	at %
Pt	81.8	58.9
Ni	16.1	38.4
In	2.1	2.6

	wt %	at %
Pt	91.4	76.4
Ni	8.5	23.5
In	0.1	0.1

	wt %	at %
Pt	79.9	54.5
Ni	20.1	45.5
In	-	-

	wt %	at %
Pt	96.5	89.4
Ni	3.5	10.6
In	-	-

Figure 7. EDS elemental mapping images and chemical compositions of catalysts before and after 12k cycles: (a) pristine In−PtNi/C, (b) In−PtNi/C after 12k cycles, (c) pristine PtNi/C, and (d) PtNi/C after 12k cycles.

PtNi/C (−71.0 mV dec^{-1}) and Pt/C (−85.8 mV dec^{-1}) (Figure 5c). These outcomes clearly demonstrate that octahedral PtNi/C has superior ORR activity to Pt/C and that the incorporation of a small amount (1.6 at. %) of In significantly improved the ORR activity of octahedral PtNi/C.

To evaluate the catalyst durability, potential cycling was conducted in the potential range of 0.6−1.1 V_{RHE} with the continuous purging of O_2 gas in a 0.1 M $HClO_4$ electrolyte with a scan rate of 50 mV s^{-1}. After 4k, 8k, and 12k cycles, the CO stripping and LSVs were measured, as shown in Figures 5d,e and Figure S8. The ECSAs and the mass and specific activities were also determined, as summarized in Table S2 and Figure 6a−c. Under the harsh durability test condition, In−PtNi/C suitably preserved the ORR performance; after the 12k cycles, the mass activity of In−PtNi/C (0.628 A mg_{Pt}^{-1}@0.9 V_{RHE}) was 2.7 and 11 times higher than those of PtNi/C (0.230 A mg_{Pt}^{-1}@0.9 V_{RHE}) and Pt/C (0.057 A mg_{Pt}^{-1}@0.9 V_{RHE}), respectively; the specific activity of In−PtNi/C (1.49 mA cm^{-2}@0.9 V_{RHE}) was 3.1 and 11.5 times higher than the corresponding values of PtNi/C (0.48 mA cm^{-2}@0.9 V_{RHE}) and Pt/C (0.130 mA cm^{-2}@0.9 V_{RHE}), respectively. The mass and specific activities of In−PtNi/C at 12k cycles were still higher than those of pristine PtNi/C and Pt/C.

To investigate the electron transfer number (n) of In−PtNi/C, ORR polarization curves of In−PtNi/C were collected in O_2-saturated 0.1 M $HClO_4$ solution with various rotation rates at a scan rate of 10 mV s^{-1} (Figure S9a). Koutechy−Levich plots (Figure S9b) obtained from the data in Figure S9a show that In−PtNi/C catalyzes the four-electron ORR pathway with an electron transfer number (n) of 4.0, indicating that the O_2 was directly reduced to H_2O. RRDE tests were also conducted to confirm the ORR kinetics (Figure S9c,d). The electron number of In−PtNi was calculated to be almost 4.0 in the potential range from 0.2 to 1.0 V_{RHE}, and the H_2O_2 yield was approximately zero, supporting direct reduction of O_2 to H_2O.

Effect of In Doping on the Stability of PtNi. The high stability of In−PtNi/C can be associated with Ni dissolution. The Ni retention capabilities of In−PtNi/C and PtNi/C (Figure 6d) were obtained from EDS composition measurements before and after 12k cycles (Figures S10−S13). In−PtNi/C exhibited only 2.4% loss of Ni, whereas PtNi/C lost 43% of Ni during the 12k cycles.

Ni retention is critical because most shape-controlled Pt-alloy nanoparticles tend to become spherical in shape depending on the diffusion barrier of Pt, as compared to other transition metals such as Ni.[25,46] Severe Ni dissolution causes poor shape stability, which in turn does not preserve the PtNi(111) facets. Figure 7 shows that doped In atoms play an important role in delaying catalytic degradation by suppressing Ni dissolution and preserving the octahedral shape. After 12k cycles, the majority of the In−PtNi nanoparticles retained their octahedral shape with the (111) facets without severe agglomeration (Figures S14 and S15), whereas most of PtNi octahedral nanoparticles lost their initial octahedral shape (in Figure S7). These results support the conclusion that In−PtNi has superior structural stability to PtNi. The commercial Pt/C also degraded in that the Pt nanoparticles increased in size due to agglomeration and/or ripening. Figures S10−S13 show the results of a low-resolution EDS analysis and the chemical compositions of numerous nanoparticles of In−PtNi/C and PtNi/C before and after 12k cycles. After 12k cycles of In−PtNi/C, the Ni composition is similar to the initial Ni at. %, and In atoms remain in the particle. On the other hand, the Ni composition in PtNi/C significantly decreased from 46.5−46.9 to 23.7−29.4 at. % during 12k cycles.

It is important to note that the In composition obtained by ICP−OES and EDS mapping is 1.6 at. %. The enhanced stability of In−PtNi octahedral nanoparticles, with such a small amount of In, can be attributed to the synthetic process; PtNi octahedral nanoparticles were prepared first and then In was incorporated. In−PtNi NPs have an average edge length of approximately 7.0 nm with an edge lattice spacing of 0.22 nm (Figure 4). Then, total number of atoms in a single NP is approximately 4579, including 685 surface atoms and 73 In atoms (1.6 at. % In). Assuming all of the In atoms are sitting on the surface of the NP,[58] In composition in the surface layer is about 11 at. %. Thus, the high surface concentration of In can effectively suppress Ni dissolution and prevent the collapse of the octahedral shape with (111) facets, resulting in excellent structural and electrochemical stability.

The stability of In should be discussed since the Pourbaix diagram indicates an oxidation state of In^{3+} under the potential cycling conditions used in this study. However, the Pourbaix diagrams consider only pure metals. If In is alloyed with other metals, In can show different behaviors from pure In. In−PtNi has negative doping energies (Figure 1), reflecting that In−PtNi is more stable than PtNi. Thus, compared to pure In, In in In−PtNi can be more resistant to dissolution. Suppression of In dissolution is experimentally observed. In content in the as-prepared In−PtNi was 1.5−1.6 at. % and lowered to 0.6−

https://doi.org/10.1021/acs.chemmater.1c03196
Chem. Mater. 2021, 33, 8895−8903

1.3 at. % after 12k potential cycles (Table S1, Figures S10 and S11). In other words, 40−80% of In survived after 12k potential cycles from 0.6 to 1.0 V_{RHE}, although In has considerably negative standard reduction potentials ($In^{3+} + 3e^- \rightarrow In$, $E^o = -0.338$ V, $In^+ + e^- \rightarrow In$, $E^o = -0.126$ V). If In behaved according to the Pourbaix diagram, In would be hardly observed after the 12k potential cycles. In addition, Ni loss from In−PtNi (2.4%) was significantly reduced compared to that from PtNi (43%), demonstrating strong interaction of In with Ni. According to a recent study,[59] In in a Pt−In−Ni alloy catalyst increased the lattice atom diffusion energy barrier and decreased the particle surface energy, improving stability of the catalyst. However, the ternary Pt−In−Ni alloy catalyst showed a relatively lower initial mass activity (0.76 A mg_{Pt}^{-1}) since the d-band center was far from the optimal value.

The white line peak in the XANES spectra is related to the electronic transition from the core $2p_{3/2}$ orbital in Pt L3 edge to the unoccupied 5d orbitals, which is sensitive to the oxidation state of Pt.[48−50] The white line peak position shifts to a lower state in the order of Pt/C > PtNi/C > In−PtNi/C in Pt L3 XANES spectra, as shown in Figure 8. The smaller

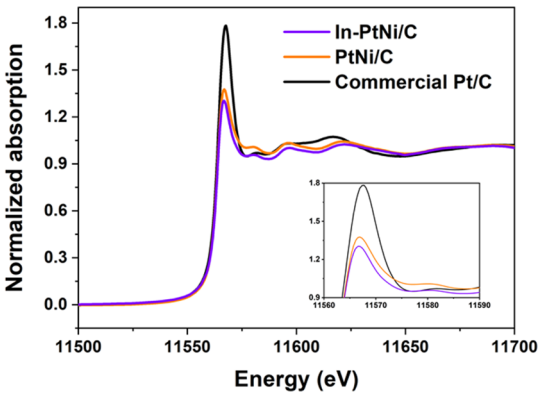

Figure 8. Pt L3 XANES spectra of In−PtNi/C, PtNi/C, and commercial Pt/C. The inset shows an enlargement of the white line peak intensity for the oxophilicity and electronic structures of Pt.

nanoparticles in the Pt/C catalyst lead to the highest bulk oxidation state due to their highest surface-to-volume ratio. In−PtNi/C has a lower oxidation state than that of PtNi/C, which implies a lower oxidation state of Pt caused by the In doping effect. This result demonstrates that In doping on the surface enhances the PtNi stability effectively by establishing a less oxidized state. The less oxidized Pt could improve the ORR kinetics and stabilize the catalysts in the durability tests.[4,60]

CONCLUSIONS

We examined the effect of surface-doped In on the properties of PtNi octahedral nanoparticles for ORR catalysis by means of a simulation and experiments. In was suggested as the most promising dopant based on the doping energy and the OH* adsorption energy as a result of dopant screening with seven different elements (Bi, In, Ru, Sn, Te, Zn, and Zr). The first nearest neighbor (1NN) Pt atoms of a doped-In atom were identified as highly active sites for the ORR because their OH* adsorption energy values are very close to the optimal value. The stability of In−PtNi was superior to that of PtNi because the presence of In increases the Ni diffusion barrier to the surface. Both In−PtNi and PtNi octahedral nanoparticles had a uniform distribution on the carbon support and exhibited a well-defined extended (111) facet. In−PtNi/C exhibited excellent ORR performance and good shape stability with high Ni retention during potential cycling tests, as compared to those of PtNi/C and commercial Pt/C. The initial mass activity of In−PtNi/C (1.36 A mg_{Pt}^{-1}@0.9 V_{RHE}) was 2.1 and 7.9 times higher than those of PtNi/C and Pt/C, respectively. The specific activity of In−PtNi/C (2.64 mA cm^{-2}@0.9 V_{RHE}) was 2.4 and 13.4 times higher than those of PtNi/C and Pt/C, respectively. After 12k cycles, In−PtNi/C was 2.7 times higher in terms of the mass activity and 3.1 times higher in terms of the specific activity, as compared to PtNi/C; this sample also showed mass activity 11 times higher and specific activity 11.5 times higher, as compared to Pt/C.

The normalized Ni content decreased only by 2.4% in the In−PtNi nanoparticles, while it decreased by 43% in the PtNi nanoparticles. After 12k cycles, the majority of In−PtNi nanoparticles retained their octahedral structure, while most of the PtNi nanoparticles became spherical. The excellent ORR performance and structural stability of the In−PtNi/C can be attributed to the lower oxophilic states made available by In doping.

In conclusion, doping In atoms into PtNi octahedral nanoparticles significantly enhances their ORR performance capabilities and structural stability, presenting In−PtNi/C as a promising ORR electrocatalyst.

ASSOCIATED CONTENT

Supporting Information

The Supporting Information is available free of charge at https://pubs.acs.org/doi/10.1021/acs.chemmater.1c03196.

Detailed experimental and computational procedures, more characterization and electrochemical details including DFT calculations, XRD, ICP−OES, TEM, EDS mapping, and additional ORR performance outcomes (PDF)

AUTHOR INFORMATION

Corresponding Authors

Graeme Henkelman − *Department of Chemistry and the Oden Institute for Computational Engineering and Science, The University of Texas at Austin, Austin, Texas 78712-1224, United States;* orcid.org/0000-0002-0336-7153; Email: henkelman@utexas.edu

EunAe Cho − *Department of Materials Science and Engineering, Korea Advanced Institute of Science and Technology (KAIST), Daejeon 34141, Republic of Korea;* orcid.org/0000-0002-2871-6903; Email: eacho@kaist.ac.kr

Authors

Jeonghoon Lim − *Department of Materials Science and Engineering, Korea Advanced Institute of Science and Technology (KAIST), Daejeon 34141, Republic of Korea;* Present Address: George W. Woodruff School of Mechanical Engineering, Georgia Institute of Technology, Atlanta, Georgia 30332, United States

Kihyun Shin − *Department of Chemistry and the Oden Institute for Computational Engineering and Science, The University of Texas at Austin, Austin, Texas 78712-1224, United States;* orcid.org/0000-0002-1748-8773

Junu Bak − *Department of Materials Science and Engineering, Korea Advanced Institute of Science and Technology (KAIST), Daejeon 34141, Republic of Korea*
JeongHan Roh − *Department of Materials Science and Engineering, Korea Advanced Institute of Science and Technology (KAIST), Daejeon 34141, Republic of Korea*
SangJae Lee − *Department of Materials Science and Engineering, Korea Advanced Institute of Science and Technology (KAIST), Daejeon 34141, Republic of Korea*

Complete contact information is available at: https://pubs.acs.org/10.1021/acs.chemmater.1c03196

Author Contributions

[§]J.L., K.S., and J.B. contributed equally.

Notes

The authors declare no competing financial interest.

■ ACKNOWLEDGMENTS

This work was supported by the National R&D Program through the National Research Foundation of Korea (NRF) funded by the Ministry of Science and ICT (NRF-2021M3H4A3A02086516 and NRF-2019M3D1A1079297). The computational work from UT Austin was supported by the Welch Foundation (F-1841) and the Texas Advanced Computing Center.

■ REFERENCES

(1) Čolić, V.; Bandarenka, A. S. Pt alloy electrocatalysts for the oxygen reduction reaction: from model surfaces to nanostructured systems. *ACS Catal.* **2016**, *6*, 5378−5385.
(2) Kim, M.; Lim, J.; Bak, J.; Song, D.; Oh, S.; Cho, E. Fe and N Codoped Mesoporous Carbon Nanofiber as a Nonprecious Metal Catalyst for Oxygen Reduction Reaction and a Durable Support for Pt Nanoparticles. *ACS Sustainable Chem. Eng.* **2019**, *7*, 17544−17552.
(3) Glüsen, A.; Dionigi, F.; Paciok, P.; Heggen, M.; Müller, M.; Gan, L.; Strasser, P.; Dunin-Borkowski, R. E.; Stolten, D. Dealloyed PtNi-core−shell nanocatalysts enable significant lowering of Pt electrode content in direct methanol fuel cells. *ACS Catal.* **2019**, *9*, 3764−3772.
(4) Kong, F.; Ren, Z.; Norouzi Banis, M.; Du, L.; Zhou, X.; Chen, G.; Zhang, L.; Li, J.; Wang, S.; Li, M.; Doyle-Davis, K.; Ma, Y.; Li, R.; Young, A.; Yang, L.; Markiewicz, M.; Tong, Y.; Yin, G.; Du, C.; Luo, J.; Sun, X. Active and Stable Pt−Ni Alloy Octahedra Catalyst for Oxygen Reduction via Near-Surface Atomical Engineering. *ACS Catal.* **2020**, *10*, 4205−4214.
(5) Li, M.; Zhao, Z.; Xia, Z.; Yang, Y.; Luo, M.; Huang, Y.; Sun, Y.; Chao, Y.; Yang, W.; Yang, W.; Yu, Y.; Lu, G.; Guo, S. Lavender-Like Ga-Doped Pt3Co Nanowires for Highly Stable and Active Electrocatalysis. *ACS Catal.* **2020**, *10*, 3018−3026.
(6) Chen, S.; Li, M.; Gao, M.; Jin, J.; van Spronsen, M. A.; Salmeron, M. B.; Yang, P. High-performance Pt−Co nanoframes for fuel-cell electrocatalysis. *Nano Lett.* **2020**, *20*, 1974−1979.
(7) Wang, D.; Xin, H. L.; Hovden, R.; Wang, H.; Yu, Y.; Muller, D. A.; DiSalvo, F. J.; Abruña, H. D. Structurally ordered intermetallic platinum−cobalt core−shell nanoparticles with enhanced activity and stability as oxygen reduction electrocatalysts. *Nat. Mater.* **2013**, *12*, 81−87.
(8) Jung, C.; Lee, C.; Bang, K.; Lim, J.; Lee, H.; Ryu, H. J.; Cho, E.; Lee, H. M. Synthesis of chemically ordered Pt3Fe/C intermetallic electrocatalysts for oxygen reduction reaction with enhanced activity and durability via a removable carbon coating. *ACS Appl. Mater. Interfaces* **2017**, *9*, 31806−31815.
(9) Han, B.; Carlton, C. E.; Suntivich, J.; Xu, Z.; Shao-Horn, Y. Oxygen reduction activity and stability trends of bimetallic Pt0. 5M0. 5 nanoparticle in acid. *J. Phys. Chem. C* **2015**, *119*, 3971−3978.
(10) Luo, M.; Guo, S. Strain-controlled electrocatalysis on multimetallic nanomaterials. *Nat. Rev. Mater.* **2017**, *2*, 17059.
(11) Wang, X.; Li, Z.; Qu, Y.; Yuan, T.; Wang, W.; Wu, Y.; Li, Y. Review of metal catalysts for oxygen reduction reaction: from nanoscale engineering to atomic design. *Chem* **2019**, *5*, 1486−1511.
(12) Kulkarni, A.; Siahrostami, S.; Patel, A.; Nørskov, J. K. Understanding catalytic activity trends in the oxygen reduction reaction. *Chem. Rev.* **2018**, *118*, 2302−2312.
(13) Jia, Q.; Li, J.; Caldwell, K.; Ramaker, D. E.; Ziegelbauer, J. M.; Kukreja, R. S.; Kongkanand, A.; Mukerjee, S. Circumventing metal dissolution induced degradation of Pt-alloy catalysts in proton exchange membrane fuel cells: revealing the asymmetric volcano nature of redox catalysis. *ACS Catal.* **2016**, *6*, 928−938.
(14) Li, Y.; Quan, F.; Chen, L.; Zhang, W.; Yu, H.; Chen, C. Synthesis of Fe-doped octahedral Pt 3 Ni nanocrystals with high electro-catalytic activity and stability towards oxygen reduction reaction. *RSC Adv.* **2014**, *4*, 1895−1899.
(15) Dionigi, F.; Weber, C. C.; Primbs, M.; Gocyla, M.; Bonastre, A. M.; Spöri, C.; Schmies, H.; Hornberger, E.; Kühl, S.; Drnec, J.; Heggen, M.; Sharman, J.; Dunin-Borkowski, R. E.; Strasser, P. Controlling near-surface Ni composition in octahedral PtNi (Mo) nanoparticles by Mo doping for a highly active oxygen reduction reaction catalyst. *Nano Lett.* **2019**, *19*, 6876−6885.
(16) Jia, Q.; Zhao, Z.; Cao, L.; Li, J.; Ghoshal, S.; Davies, V.; Stavitski, E.; Attenkofer, K.; Liu, Z.; Li, M.; Duan, X.; Mukerjee, S.; Mueller, T.; Huang, Y. Roles of Mo surface dopants in enhancing the ORR performance of octahedral PtNi nanoparticles. *Nano Lett.* **2018**, *18*, 798−804.
(17) Lim, J.; Shin, H.; Kim, M.; Lee, H.; Lee, K.-S.; Kwon, Y.; Song, D.; Oh, S.; Kim, H.; Cho, E. Ga−Doped Pt−Ni Octahedral Nanoparticles as a Highly Active and Durable Electrocatalyst for Oxygen Reduction Reaction. *Nano Lett.* **2018**, *18*, 2450−2458.
(18) Beermann, V.; Gocyla, M.; Willinger, E.; Rudi, S.; Heggen, M.; Dunin-Borkowski, R. E.; Willinger, M.-G.; Strasser, P. Rh-doped Pt−Ni octahedral nanoparticles: understanding the correlation between elemental distribution, oxygen reduction reaction, and shape stability. *Nano Lett.* **2016**, *16*, 1719−1725.
(19) Kan, D.; Lian, R.; Wang, D.; Zhang, X.; Xu, J.; Gao, X.; Yu, Y.; Chen, G.; Wei, Y. Screening effective single-atom ORR and OER electrocatalysts from Pt decorated MXenes by first-principles calculations. *J. Mater. Chem. A* **2020**, *8*, 17065−17077.
(20) Nagaprasad Reddy, S.; Krishnamurthy, C. B.; Grinberg, I. First-Principles Study of the Ligand Substituent Effect on ORR Catalysis by Metallocorroles. *J. Phys. Chem. C* **2020**, *124*, 11275−11283.
(21) Wan, H.; Jensen, A. W.; Escudero-Escribano, M.; Rossmeisl, J. Insights in the oxygen reduction reaction: from metallic electrocatalysts to diporphyrins. *ACS Catal.* **2020**, *10*, 5979−5989.
(22) Rebarchik, M.; Bhandari, S.; Kropp, T.; Mavrikakis, M. How Noninnocent Spectator Species Improve the Oxygen Reduction Activity of Single-Atom Catalysts: Microkinetic Models from First-Principles Calculations. *ACS Catal.* **2020**, *10*, 9129−9135.
(23) Galyamova, A.; Shin, K.; Henkelman, G.; Crooks, R. M. Effect of TiO x Substrate Interactions on the Electrocatalytic Oxygen Reduction Reaction at Au Nanoparticles. *J. Phys. Chem. C* **2020**, *124*, 10045−10056.
(24) Lee, C.; Shin, K.; Jung, C.; Choi, P.-P.; Henkelman, G.; Lee, H. M. Atomically Embedded Ag via Electrodiffusion Boosts Oxygen Evolution of CoOOH Nanosheet Arrays. *ACS Catal.* **2019**, *10*, 562−569.
(25) Gamler, J. T. L.; Shin, K.; Ashberry, H. M.; Chen, Y.; Bueno, S. L. A.; Tang, Y.; Henkelman, G.; Skrabalak, S. E. Intermetallic Pd 3 Pb nanocubes with high selectivity for the 4-electron oxygen reduction reaction pathway. *Nanoscale* **2020**, *12*, 2532−2541.
(26) Zhong, L.; Li, S. Unconventional oxygen reduction reaction mechanism and scaling relation on single-atom catalysts. *ACS Catal.* **2020**, *10*, 4313−4318.
(27) Zhao, Y.; Wang, X.; Cheng, G.; Luo, W. Phosphorus-Induced Activation of Ruthenium for Boosting Hydrogen Oxidation and Evolution Electrocatalysis. *ACS Catal.* **2020**, *10*, 11751−11757.
(28) Luo, F.; Roy, A.; Silvioli, L.; Cullen, D. A.; Zitolo, A.; Sougrati, M. T.; Oguz, I. C.; Mineva, T.; Teschner, D.; Wagner, S.; Wen, J.;

Dionigi, F.; Kramm, U. I.; Rossmeisl, J.; Jaouen, F.; Strasser, P. P-block single-metal-site tin/nitrogen-doped carbon fuel cell cathode catalyst for oxygen reduction reaction. *Nat. Mater.* **2020**, *19*, 1215−1223.
(29) Hammer, B.; Hansen, L. B.; Nørskov, J. K. Improved adsorption energetics within density-functional theory using revised Perdew-Burke-Ernzerhof functionals. *Phys. Rev. B: Condens. Matter Mater. Phys.* **1999**, *59*, 7413.
(30) Zhang, Y.; Yang, W. Comment on "Generalized gradient approximation made simple". *Phys. Rev. Lett.* **1998**, *80*, 890.
(31) Perdew, J. P.; Burke, K.; Ernzerhof, M. Generalized gradient approximation made simple. *Phys. Rev. Lett.* **1996**, *77*, 3865.
(32) Rossmeisl, J.; Karlberg, G. S.; Jaramillo, T.; Nørskov, J. K. Steady state oxygen reduction and cyclic voltammetry. *Faraday Discuss.* **2009**, *140*, 337−346.
(33) Stephens, I. E. L.; Bondarenko, A. S.; Grønbjerg, U.; Rossmeisl, J.; Chorkendorff, I. Understanding the electrocatalysis of oxygen reduction on platinum and its alloys. *Energy Environ. Sci.* **2012**, *5*, 6744−6762.
(34) Seh, Z. W.; Kibsgaard, J.; Dickens, C. F.; Chorkendorff, I.; Nørskov, J. K.; Jaramillo, T. F. Combining theory and experiment in electrocatalysis: Insights into materials design. *Science* **2017**, *355*, No. eaad4998.
(35) Huang, Z.-F.; Wang, J.; Peng, Y.; Jung, C.-Y.; Fisher, A.; Wang, X. Design of efficient bifunctional oxygen reduction/evolution electrocatalyst: recent advances and perspectives. *Adv. Energy Mater.* **2017**, *7*, 1700544.
(36) Zhou, R.; Zheng, Y.; Jaroniec, M.; Qiao, S.-Z. Determination of the electron transfer number for the oxygen reduction reaction: from theory to experiment. *ACS Catal.* **2016**, *6*, 4720−4728.
(37) Liu, Z.; Zhao, Z.; Peng, B.; Duan, X.; Huang, Y. Beyond Extended Surfaces: Understanding the Oxygen Reduction Reaction on Nanocatalysts. *J. Am. Chem. Soc.* **2020**, *142*, 17812−17827.
(38) Cui, C.; Gan, L.; Heggen, M.; Rudi, S.; Strasser, P. Compositional segregation in shaped Pt alloy nanoparticles and their structural behaviour during electrocatalysis. *Nat. Mater.* **2013**, *12*, 765−771.
(39) Beermann, V.; Gocyla, M.; Kühl, S.; Padgett, E.; Schmies, H.; Goerlin, M.; Erini, N.; Shviro, M.; Heggen, M.; Dunin-Borkowski, R. E.; Muller, D. A.; Strasser, P. Tuning the electrocatalytic oxygen reduction reaction activity and stability of shape-controlled Pt−Ni nanoparticles by thermal annealing− elucidating the surface atomic structural and compositional changes. *J. Am. Chem. Soc.* **2017**, *139*, 16536−16547.
(40) Liu, M.; Zhao, Z.; Duan, X.; Huang, Y. Nanoscale structure design for high-performance Pt-based ORR catalysts. *Adv. Mater.* **2019**, *31*, 1802234.
(41) Zhu, J.; Jiang, X.; Yang, Y.; Chen, Q.; Xue, X.-X.; Chen, K.; Feng, Y. Synergy of tellurium and defects in control of activity of phosphorene for oxygen evolution and reduction reactions. *Phys. Chem. Chem. Phys.* **2019**, *21*, 22939−22946.
(42) Li, J.; Chen, S.; Yang, N.; Deng, M.; Ibraheem, S.; Deng, J.; Li, J.; Li, L.; Wei, Z. Ultrahigh-loading zinc single-atom catalyst for highly efficient oxygen reduction in both acidic and alkaline media. *Angew. Chem., Int. Ed.* **2019**, *58*, 7035−7039.
(43) Wang, X.; Li, X.; Liao, S.; Li, B. DFT study of high performance Pt3Sn alloy catalyst in oxygen reduction reaction. *Comput. Mater. Sci.* **2018**, *149*, 107−114.
(44) Zhang, B.-W.; Lai, W.-H.; Sheng, T.; Qu, X.-M.; Wang, Y.-X.; Ren, L.; Zhang, L.; Du, Y.; Jiang, Y.-X.; Sun, S.-G.; Dou, S.-X. Ordered platinum−bismuth intermetallic clusters with Pt-skin for a highly efficient electrochemical ethanol oxidation reaction. *J. Mater. Chem. A* **2019**, *7*, 5214−5220.
(45) Nandi, S.; Nair, A. S.; Pathak, B. First principles investigation on the applicability of ruthenium as a potential ORR catalyst. *J. Chem. Sci.* **2020**, *132*, 2.
(46) Cheng, Y.; Zhao, X.; Yu, Y.; Chen, L.; Cheng, T.; Huang, J.; Liu, Y.; Harada, M.; Ishihara, A.; Wang, Y. Indium oxide supported Pt−In alloy nanocluster catalysts with enhanced catalytic performance toward oxygen reduction reaction. *J. Power Sources* **2020**, *446*, 227332.
(47) Nørskov, J. K.; Rossmeisl, J.; Logadottir, A.; Lindqvist, L.; Kitchin, J. R.; Bligaard, T.; Jonsson, H. Origin of the overpotential for oxygen reduction at a fuel-cell cathode. *J. Phys. Chem. B* **2004**, *108*, 17886−17892.
(48) Bajdich, M.; García-Mota, M.; Vojvodic, A.; Nørskov, J. K.; Bell, A. T. Theoretical investigation of the activity of cobalt oxides for the electrochemical oxidation of water. *J. Am. Chem. Soc.* **2013**, *135*, 13521−13530.
(49) Man, I. C.; Su, H. Y.; Calle-Vallejo, F.; Hansen, H. A.; Martínez, J. I.; Inoglu, N. G.; Kitchin, J.; Jaramillo, T. F.; Nørskov, J. K.; Rossmeisl, J. Universality in oxygen evolution electrocatalysis on oxide surfaces. *ChemCatChem* **2011**, *3*, 1159−1165.
(50) Stamenkovic, V. R.; Fowler, B.; Mun, B. S.; Wang, G.; Ross, P. N.; Lucas, C. A.; Marković, N. M. Improved oxygen reduction activity on Pt3Ni (111) via increased surface site availability. *Science* **2007**, *315*, 493−497.
(51) Choi, J.; Lee, Y.; Kim, J.; Lee, H. Enhancing stability of octahedral PtNi nanoparticles for oxygen reduction reaction by halide treatment. *J. Power Sources* **2016**, *307*, 883−890.
(52) Kim, S. K.; Shin, K.; Henkelman, G. Stability of Pt Skin Intermetallic Core Catalysts and Adsorption Properties for the Oxygen Reduction Reaction. *J. Phys. Chem. C* **2021**, *125*, 3527−3534.
(53) Tripkovic, V.; Vegge, T. Potential-and rate-determining step for oxygen reduction on Pt (111). *J. Phys. Chem. C* **2017**, *121*, 26785−26793.
(54) Hansen, M. H.; Nilsson, A.; Rossmeisl, J. Modelling pH and potential in dynamic structures of the water/Pt(111) interface on the atomic scale. *Phys. Chem. Chem. Phys.* **2017**, *19*, 23505−23514.
(55) Dix, S. T.; Linic, S. In-operando surface-sensitive probing of electrochemical reactions on nanoparticle electrocatalysts: Spectroscopic characterization of reaction intermediates and elementary steps of oxygen reduction reaction on Pt. *J. Catal.* **2021**, *396*, 32−39.
(56) Rudi, S.; Cui, C.; Gan, L.; Strasser, P. Comparative Study of the Electrocatalytically Active Surface Areas (ECSAs) of Pt Alloy Nanoparticles Evaluated by Hupd and CO-stripping voltammetry. *Electrocatalysis* **2014**, *5*, 408−418.
(57) van der Vliet, D. F.; Wang, C.; Li, D.; Paulikas, A. P.; Greeley, J.; Rankin, R. B.; Strmcnik, D.; Tripkovic, D.; Markovic, N. M.; Stamenkovic, V. R. Unique Electrochemical Adsorption Properties of Pt -SkinSurfaces. *Angew. Chem., Int. Ed.* **2012**, *51*, 3139.
(58) Huang, X.; Zhao, Z.; Cao, L.; Chen, Y.; Zhu, E.; Lin, Z.; Li, M.; Yan, A.; Zettl, A.; Wang, Y. M.; Duan, X.; Mueller, T.; Huang, Y. High-performance transition metal−doped Pt3Ni octahedra for oxygen reduction reaction. *Science* **2015**, *348*, 1230−1234.
(59) Shen, X.; Dai, S.; Pan, Y.; Yao, L.; Yang, J.; Pan, X.; Zeng, J.; Peng, Z. Tuning Electronic Structure and Lattice Diffusion Barrier of Ternary Pt−In−Ni for Both Improved Activity and Stability Properties in Oxygen Reduction Electrocatalysis. *ACS Catal.* **2019**, *9*, 11431−11437.
(60) Zhang, J.; Yuan, Y.; Gao, L.; Zeng, G.; Li, M.; Huang, H. Stabilizing Pt-Based Electrocatalysts for Oxygen Reduction Reaction: Fundamental Understanding and Design Strategies. *Adv. Mater.* **2021**, *33*, 2006494.

https://doi.org/10.1021/acs.chemmater.1c03196
Chem. Mater. 2021, 33, 8895−8903